The Exact Morphology of Metal Organic Framework MIL-53(Fe) Influences its Photocatalytic Performance

H. Pazhand [a,b], A.A. Sabbagh Alvani [a,b,c*], H. Sameie [b,c], R. Salimi [b,c], D. Poelman [d]

Hooman Pazhand, Prof. Ali Asghar sabbagh Alvani, Dr. Hassan Sameie, Dr.Reza Salimi , Prof. Dirk Poelman

[a] Department of Polymer Engineering & Color Technology, Amirkabir University of Technology, Tehran 1591634311, Iran

[b] Color & Polymer Research Center (CPRC), Amirkabir University of Technology, Tehran 1591634311, Iran

[c] Standard Research Institute, Alborz 3174734563, Iran

[d] Department of Solid State Sciences, Lumilab, Ghent University, Krijgslaan 281-S1, 9000 Ghent, Belgium

https://doi.org/10.21203/rs.3.rs-2025694/v1/

* **Corresponding author:**

E-mail: sabbagh_alvani@aut.ac.ir

Abstract

Controllable synthesis of Metal-organic frameworks (MOFs) with well-defined morphology, composition and size is of great importance towards understanding their structure-property relationship in various applications. Herein, the effect of morphology of photocatalysts on their optical behavior and photocatalytic efficiency was identified utilizing physical synthetic parameters for methylene blue removal. For this purpose, MIL-53(Fe) was fabricated as an efficient photocatalyst via solvothermal approach using chloride and nitrate salts as different secondary block unit (SBU) sources. Each of the powders obtained by two metal sources was synthesized at three different temperatures (120, 150, and 180 ºC). The fabricated MOFs were methodically investigated and characterized in terms of structural, textural, morphological and optical. The obtained empirical data confirmed that the particles synthesized at 120 ºC using iron chloride exhibit the highest efficiency for methylene blue removal. This could be associated to their high surface area and UV light absorption in comparison with other samples. These results can be considered in future research to maximize degradation of organic dyes as a serious pollutant in wastewater.

Introduction

The increasing demand of clean water sources and its shortage due to the rapid development of industrialization and population growth have prompted researchers to cope with this issue. Many water treatment technologies such as adsorption or coagulation have been utilized to purify water effectively, but pollutants still remain and they are not completely eliminated due to the lack of adequate efficiency of most treatment methods [1]. Therefore, research has been carried out to find more efficient techniques for wastewater treatment. Among various physical, chemical, and biological technologies used in pollution control, advanced oxidation processes (AOPs) are selected for destruction of organic contaminants, due to their high efficiency, simplicity, good reproducibility and easy handling [2].

Metal-Organic Frameworks (MOFs) are types of coordination polymers with diverse structures increasingly considered in AOP process due to their fascinating properties [3]. These multi- structure polymers can be utilized in a wide range of applications and they are known as candidates for gas storage [4], optical devices [5], absorbent [6], sensor application [7], photocatalyst [8] and drug delivery [9] due to their facile synthesis, ultrahigh specific surface area, and high porosity.

In recent years, many MOFs are being employed for photocatalytic application and MOF-5 was the first one used to depollute organic dyes from wastewater [10]. There have been numerous MOFs synthesized since two decades ago. Iron containing MOFs have been considered to be used for photocatalytic applications not only due to their satisfactory photocatalytic performance but also because of involving Fenton process [11]. Furthermore, Fe-based MILs are visible-light responsive because of the presence of iron-oxo (Fe-O) clusters. It has been demonstrated that the (Fe-O) clusters can contribute to electron excitation [12]. Many reports have investigated the effects of synthesis parameters on photocatalytic and catalytic activity of iron containing MOFs. For instance, Wang et al. synthesized MIL-88(A) at different times and temperatures to optimize the catalytic activity of obtained powders for persulfate activation [13]. Viswanathan et al. investigated the effects of different solvents on morphology of MIL-88(A). Subsequently, the effects of this variable on photocatalytic performance of the powders were analyzed using a comprehensive set of analyses [14]. Pu et al. demonstrated that different synthesis conditions of MIL-53(Fe) can affect the catalytic performance [15].

In the present study, new parameters were investigated to improve the MIL-53(Fe) photocatalytic activity. MIL-53(Fe) was obtained using nitrate and chloride salts as synthesis sources. Moreover, each of the powders was synthesized at three different temperatures. Finally, photonic performance of the obtained powders was analyzed comprehensively through methylene blue (MB) degradation as one of the prevalent organic pollutants.

Results and discussion

The XRD patterns of all samples are shown in Figure 1. The results revealed that despite intensity differences, the XRD patterns of samples (C), (D), (E), and (F) showed sharp and strong peaks. According to the XRD patterns of the above mentioned samples, the samples were successfully synthesized with high crystallinity. In addition, the strong peaks of the samples were at the same positions (9.2º, 10.1º, 12.6º, 18.5º, 25.2º), indicating that these four samples consisted of the same phase. Likewise, Figure 1 illustrated that sample (A) and sample (B) only had low intensity and wide peaks, pointing to an amorphous structure. The XRD patterns are concordant with those presented in the literatures [16].

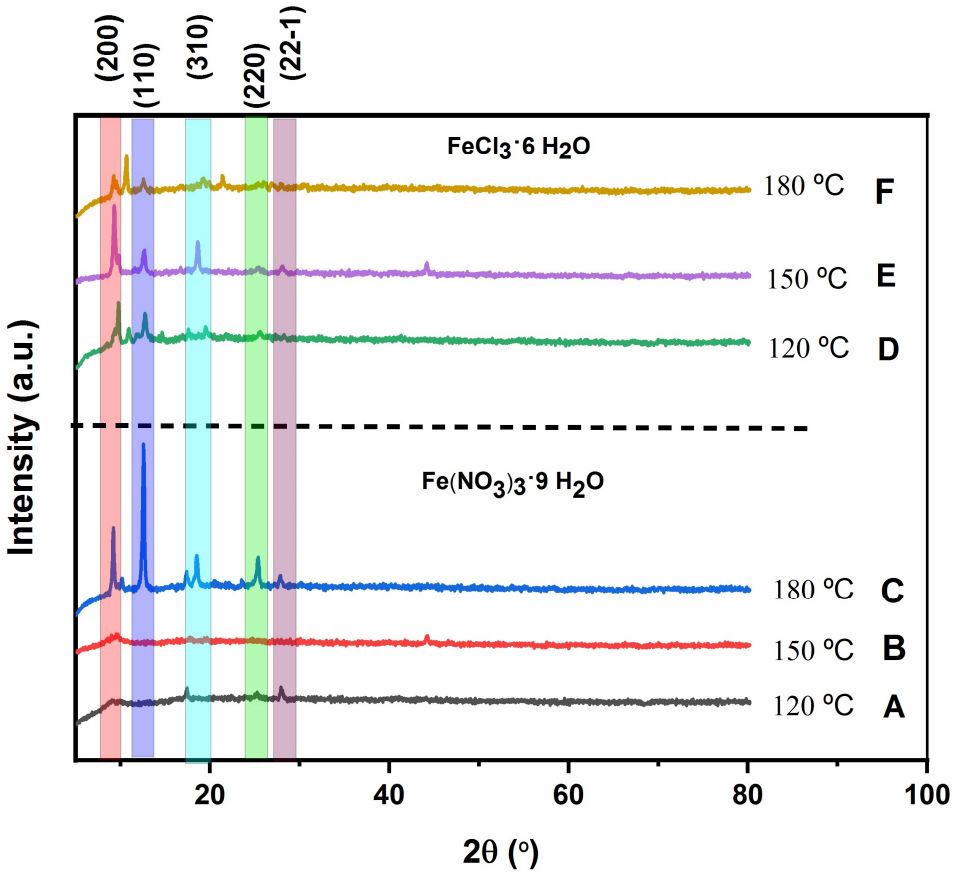

Figure 1. XRD patterns of MIL-53(Fe) synthesized using different preparation conditions

FT-IR analysis was used to examine the structure of the samples. The characteristic absorption peaks were observed at 560.84 cm^{-1}, 749.01 cm^{-1}, 1390.01 cm^{-1}, 1599.42 cm^{-1} and 1659.81 cm^{-1} which is associated with carboxylate groups. The sharp absorption peaks at 560.84 cm^{-1} are related to vibration of Fe-O as metal-oxygen bonding. The strong peaks at 1390.01 cm^{-1} and 1599.42 cm^{-1} are attributed to symmetric and asymmetric structure of C-O in carboxyl groups. The peak at 749.01 cm^{-1} is

ascribed to C-H bending vibration of benzene rings. FT-IR spectra of samples corresponded to the results presented in the literature [17].

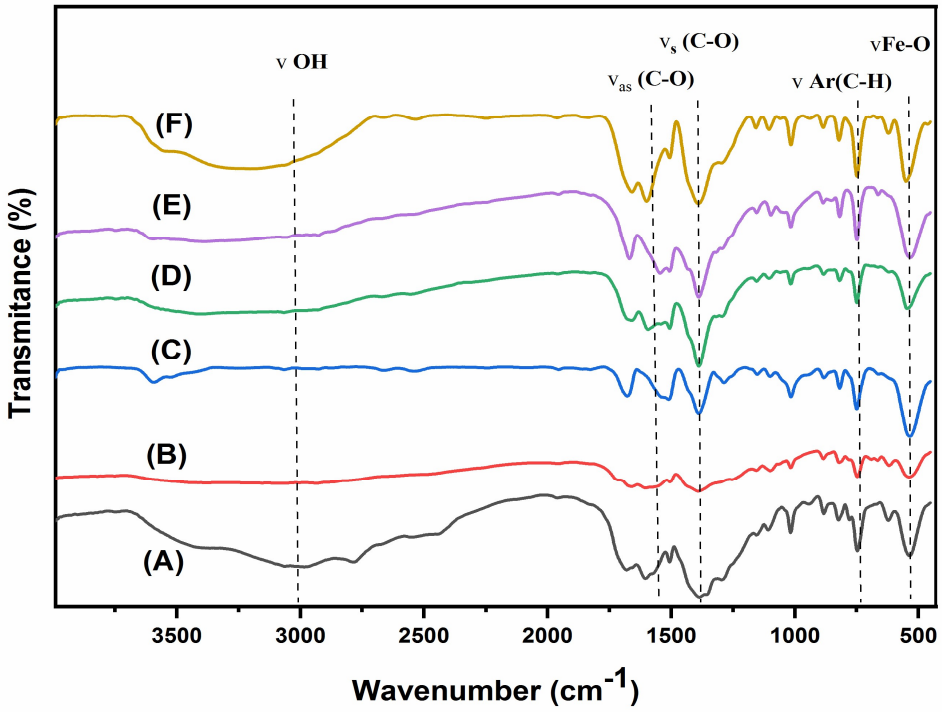

Figure 2. FT-IR spectra of as-prepared photocatalysts (nitrate salt: A 120 ºC/ B 150 ºC/ C 180 ºC) and (chloride salt: D 120 ºC/ E 150 ºC/ F 180 ºC)

SEM analysis was carried out to evaluate the morphology of the samples. SEM images illustrate that particle sizes of samples (A) and (B) were considerably higher than those of other samples. This can be traced to the amorphous structure of these samples. Also, SEM images indicate that synthesis temperature significantly affected the morphology of the powders. It was found that by increasing the temperature to 180 ºC, the morphology of sample (C) was completely changed and converted to the MIL-88A structure reported by previous studies [18]. The powders synthesized at 120 ºC (Figure 3D) and 150 ºC (Figure 3E) had heterogeneous particles with two morphologies. In addition, sample (D) and sample (E) consisted of plates with non-regular shapes and small spherical crystals that did not adequately grow. This heterogeneity observed in particles size distribution can be attributed to poor heat transfer at a lower temperature. As a result, concurrent nucleation and crystal growth can intervene at such temperatures [19]. In case of sample E, spherical crystals grew and changed into a hexagonal bipyramid morphology. By increasing temperature to 180 ºC, the morphology of sample (F) slightly differed so that bigger bipyramid crystals with a more homogenous distribution were achieved.

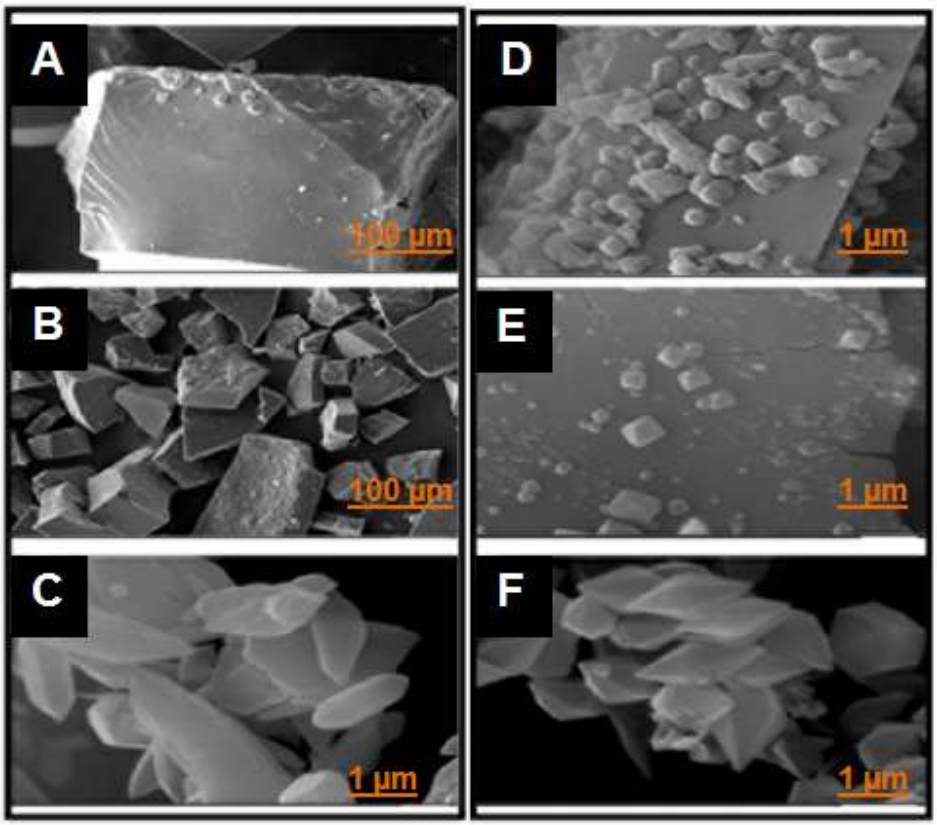

Figure 3. SEM images of MIL-53(Fe)-Nitrate salt/120 ºC (A), MIL-53(Fe)-Nitrate salt/150 ºC (B), MIL-53(Fe)- Nitrate salt/180 ºC (C), MIL-53(Fe)-Chloride salt/120 ºC (D), MIL-53(Fe)-Chloride salt/150 ºC (E), MIL-53(Fe)-Chloride salt/180 ºC (F)

Particle size of MIL-53(Fe) was measured by DLS method. As shown in Fig.4 the average particle size is 1353 nm for sample (C), 1019 nm for sample (D), 977 nm for sample (E) and 1000 nm for sample (F). (DLS analysis could not be utilized for sample (A,B) due to their large particle size). The data showed that changing in nitrite salt to chloride salt decreases the particle size. This decrease in the size is confirmed by SEM images (Figure 4)

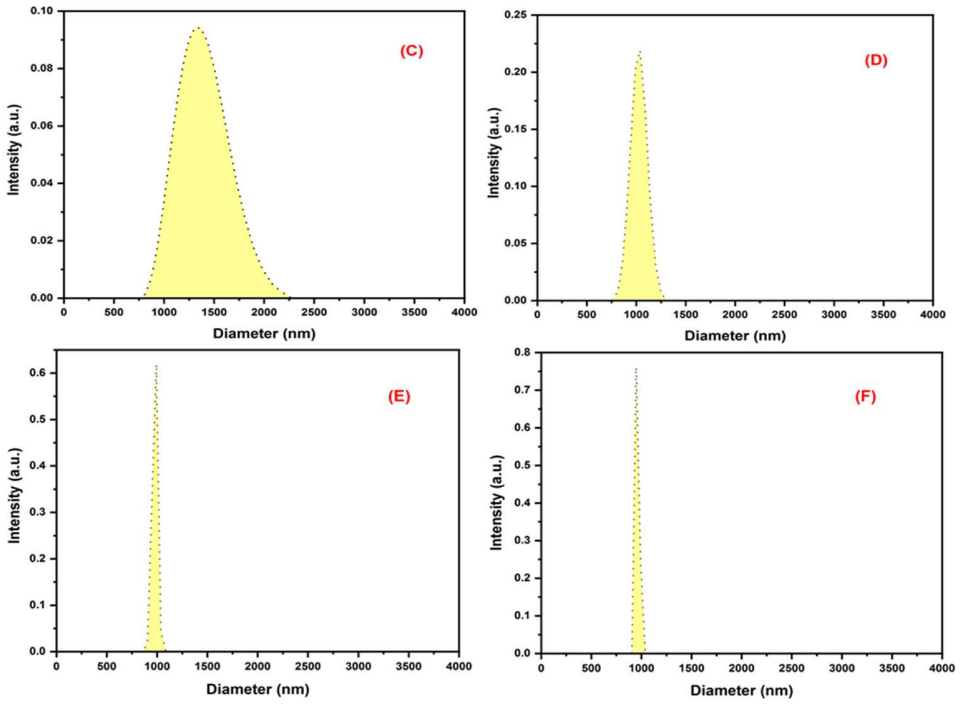

Figure 4. DLS results for MIL-53(Fe)- Nitrate salt/180 ºC (C), MIL-53(Fe)-Chloride salt/120 ºC (D), MIL-53(Fe)-Chloride salt/150 ºC (E), MIL-53(Fe)-Chloride salt/180 ºC (F)

To study optical properties of the particles, UV-Vis DRS was utilized. As observed in Figure 5, all synthesized powders showed strong visible light absorption at a wavelength of 441 nm. Consequently, these photocatalysts are capable of being used in the range of visible spectrum. Furthermore, light response at this wavelength is ascribed to the transition ([$^6A_{1g}$ $^4A_{1g}$ +^{4} Eg→ (G)]) in Fe(III) [20]. According to Figure 5, sample (D) had the highest absorption among the samples. To calculate the MIL-53(Fe) band gap energy, the Tauc equation (Eqn (1)) was utilized.

$$\alpha h\upsilon = A(h\upsilon - E_g)^n \qquad (1)$$

where *h* is the Planck constant; *A* is a constant value; *α* and *v* are diffuse absorption coefficient and light frequency, respectively [21]. According to the results, samples (A) and (B) have lower band gap energy (E_g) (1.9 eV) in comparison to other samples. However, estimated band gap energy of samples (C), (D), (E), and (F) was 2.85 eV. The obtained results for sample (C), (D), (E) and (F) confirms the same values with those reported for MIL-53(Fe) in previous studies (the order was approximately between 2.6 to 2.8) [16(c,d) , 17c] . The difference between the bandgap value of the samples (A) and (B) with other samples can be attributed to amorphous structure of sample (A) and (B) [22]. Approximate band gap of samples was obtained by the tangent to the curve of $(\alpha hv)^2$ vs. photo energy (Figure 6 a,b).

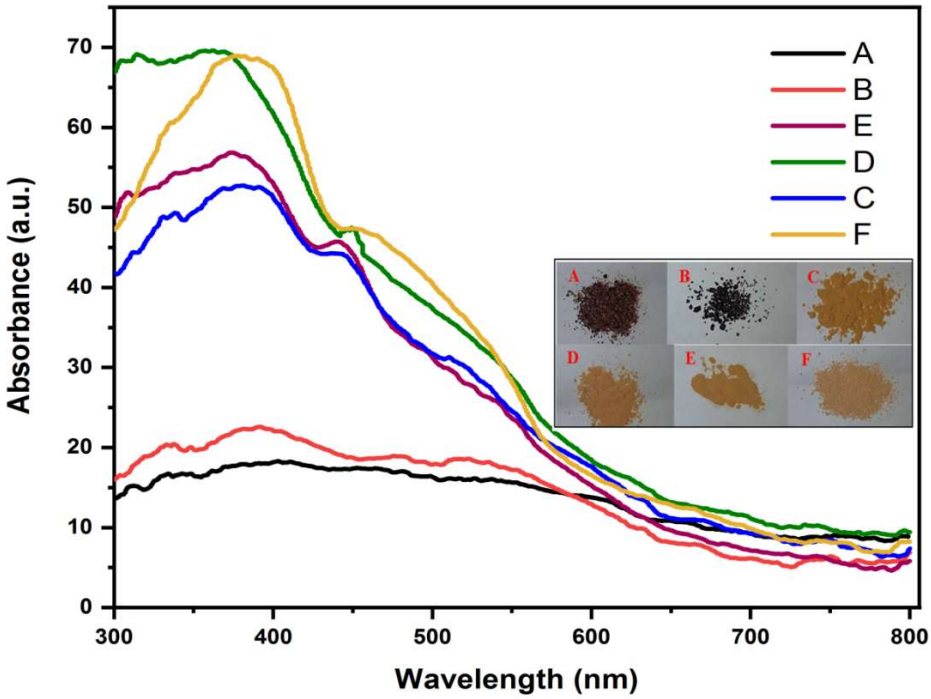

Figure 5. UV-vis diffuse reflectance spectra of the prepared photocatalysts A) Nitrate salt/120 ºC, B) Nitrate salt/150 ºC, C) Nitrate salt/180 ºC, D) Chloride salt/120 ºC, E) Chloride salt/150 ºC, F) Chloride salt/180 ºC

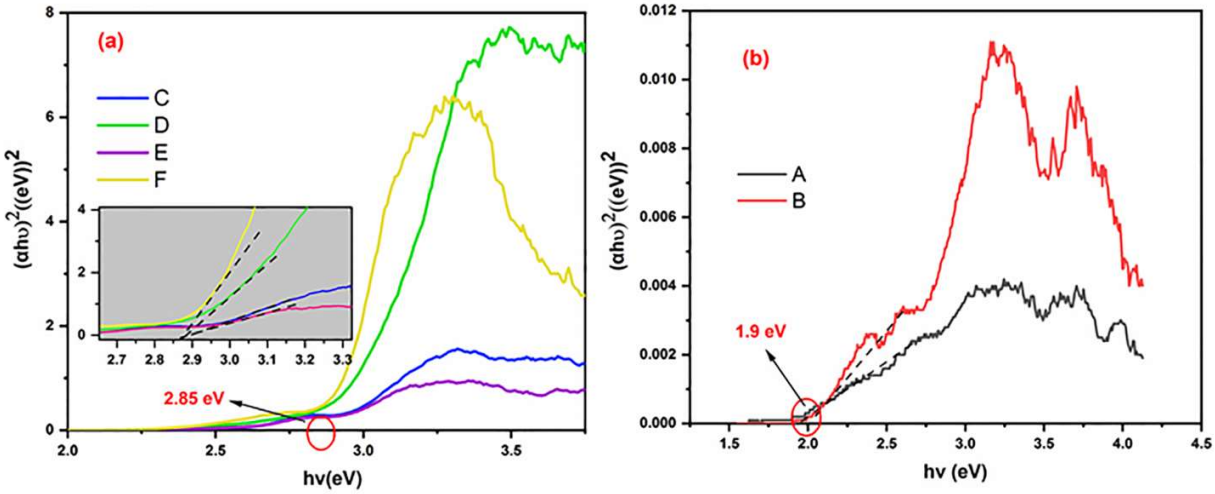

Figure 6. Plot of $(\alpha h\nu)^2$ vs. photon energy (hv) of MIL-53(Fe)

To study specific surface area of the powders, BET analysis was performed. Figure 7 illustrates N_2 adsorption/desorption isotherms of sample (D), and the corresponding pore size distribution (PSD) is shown in the inset (BJH adsorption dv_p/dr_p pore volume). Two strong peaks can be observed at 8 and 34 nm, and pore sizes in the range of 2-50 nm were dominant. Also,

pores within sample (D) were mesoporous which have a vital role for improving photocatalytic performance of particles [23]. In addition, N_2 adsorption/desorption isotherm observed for sample (D) represents a IV-type adsorption curve and the hysteresis loop can be attributed to type H3, displaying slit-like mesopores/macropores in the powder [24]. Table 1 presents the total pore volume and surface area of particles resulting from BET analysis for all samples. According to Table 1, S_{BET} of sample (B) is higher than that of sample (C). This is due to the amorphous structure of sample (B) which was confirmed by XRD patterns. Considering the mechanism of BET analysis, S_{BET} values are associated with adsorption of N_2 molecules in the particle structure. If particles are amorphous, penetration of N_2 molecules is more feasible. Thus, the result obtained for sample (B) cannot be considered as the real amount of specific surface area for this sample. The BET analysis confirms that there is correspondence between the obtained results in recent study and reported data in previous literatures[12,15].

Table 1. BET of powders synthesized in different conditions

Sample	S_{BET} (m^2/g)	Total pore volume (cm^3g^{-1})	Mean pore diameter (nm)
A	2.3	0.006	11.29
B	6.6	0.021	12.8
C	3.8	0.016	17.47
D	23.06	0.114	19.79
E	6.05	0.026	17.74
F	10.05	0.025	9.66

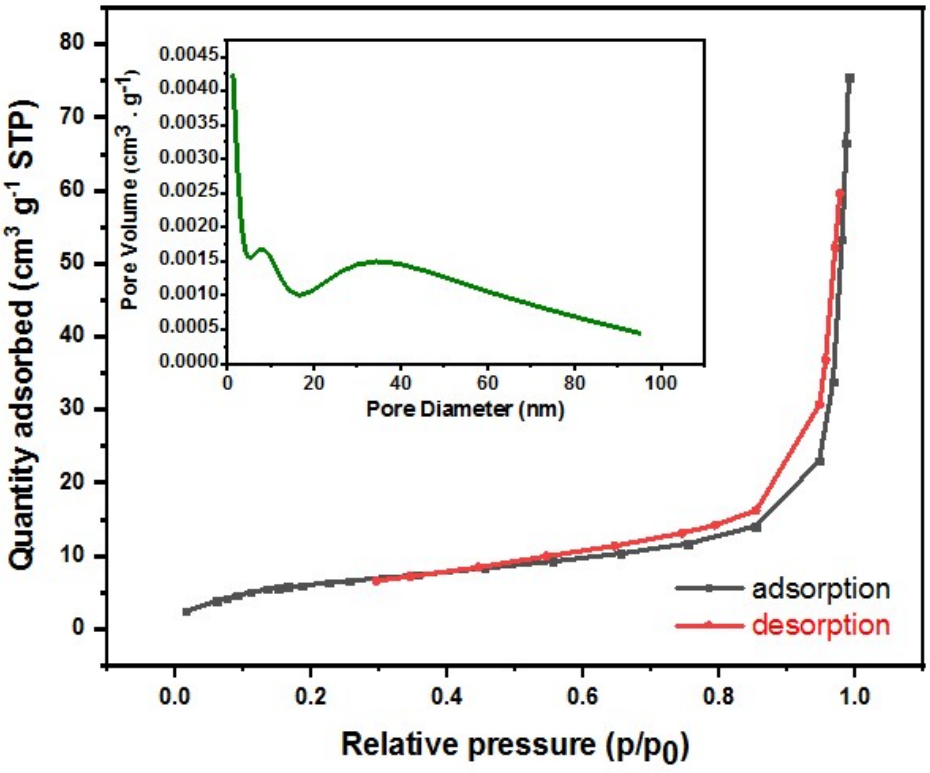

Figure 7. N_2 adsorption/desorption isotherms of MIL53-(Fe) prepared with chloride salt at 120 ºC (sample D) (inset shows the pore size distribution of particles in sample (D)

MB removal using different synthesized photocatalysts

To investigate the photocatalytic performance of the powders, a certain amount of each synthesized photocatalyst was utilized in MB solution. Figure 8 shows the adsorption and degradation of MB as a function of time in ambient conditions in the presence of different types of photocatalysts. Initially, dye removal through adsorption in the dark was analyzed to evaluate the amount of dye extracted via adsorption by photocatalysts powders. Furthermore, to clarify MB degradation in the presence of H_2O_2, dye solutions were put at ambient condition with a certain amount of H_2O_2 without any photocatalysts. Results indicated that dye adsorption enhanced by increasing the surface area of samples. In other words, dye adsorption is directly related to the surface area of the powders. Moreover, results revealed that H_2O_2 slightly degraded the dye (< 5% of dye concentration). Therefore, despite the role of hydrogen peroxide in dye degradation, it cannot be considered as a significant parameter for this purpose. Furthermore, the data from Fig.8 shows that, under visible light irradiation, the solution consisted of sample (D)/MB without any amount of H_2O_2 was capable to degrade MB approximately 33%.However, Figure 8 demonstrates that the photocatalysts increasingly affected dye degradation and had more contribution to this process. Figure

8 also shows that different preparation conditions not only have a vital effect on adsorption but also can considerably influence the rate of degradation. As can be observed in this figure, photocatalysts synthesized in different conditions exhibited different performances. Sample (D) had the best performance and effectively degraded the dye. However, samples (A) and (B) showed the weakest efficiency and could not degrade MB adequately. This may be due to the amorphous structure of these two samples. Hence, their light absorbance was lower than the minimum needed for electron excitation and subsequently be activated to perform as a photocatalyst. The rate of MB degradation for different photocatalysts is in the following order: sample (D) > sample (F) > sample (E) > sample (C) > sample (A) = sample (B).

Considering the results, dye degradation was directly related to S_{BET} for successfully synthesized crystals (C, D, E and F). As a result, S_{BET} has a considerable effect on adsorption and degradation simultaneously so that the sample with higher S_{BET} has higher dye degradation efficiency[13,15], as can be observed in Figure 8. In general, according to numerous studies, the Langmuir-Hinshelwood (L-H) mechanism has been successfully used to specify the relation between the initial rate of dye degradation ($-r_A$) and initial dye concentration (C_A) [25]. The modified L-H equation is given by Eqn (2):

$$r = \frac{dc}{dt} = k_r\,\theta = \frac{k_r KC}{1+KC} \qquad (2)$$

where k_r is the reaction rate constant, K is reactant adsorption constant, θ is the fraction of MIL-53(Fe) surface coverage, and C is the concentration of MB at time t. When the organic concentration is low enough, a pseudo-first-order kinetic model can be applied [26]. In this study, pseudo-first-order and pseudo-second-order models were simultaneously utilized to compare and study the adsorption as well as dye degradation isotherm comprehensively. Obtained data are illustrated in Figure 9. It is shown that the pseudo-first-order (Eqn (3)) model appropriately fitted to the data due to a higher value of R^2.

$$Ln\left(\frac{C_0}{C}\right) = k_r K\, t = k_{app} t \qquad (3)$$

where $K_{app} = k_r K$ and C_0 is the initial concentration of MB.

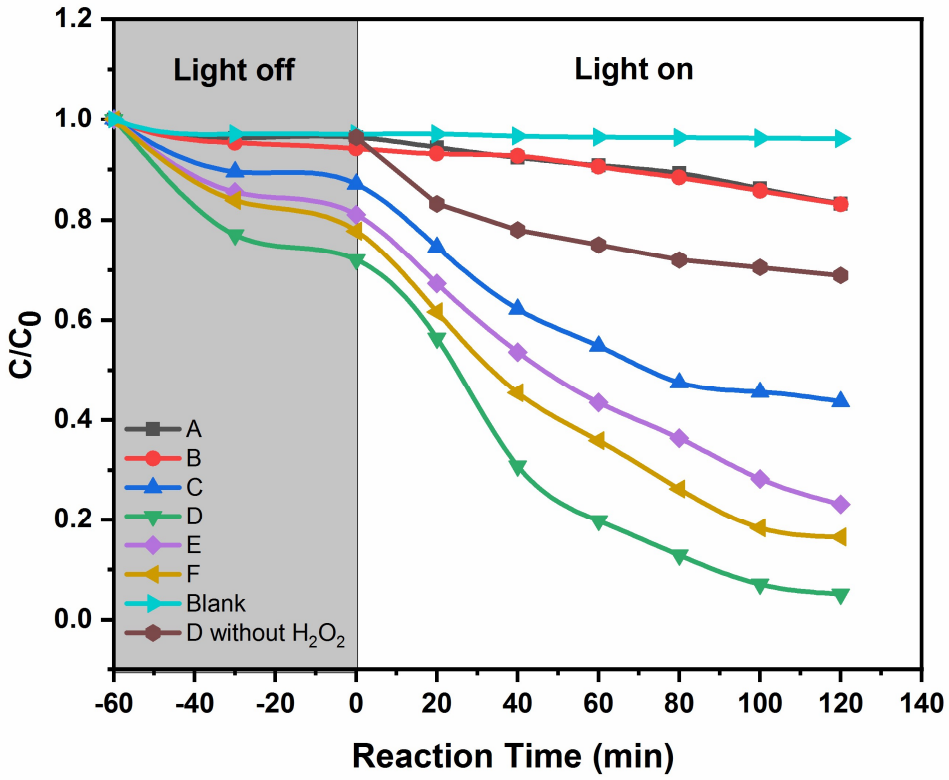

Figure 8. Photocatalytic activities of photocatalysts on the degradation of methylene blue

The sample synthesized using chloride salt at 120 ºC (sample (D)) had the highest value of K (K = 0/03) among the samples which was three times higher than that of sample (F). Also, sample (C) had a lower dye degradation rate than samples (D), (E), and (F) due to lower dispersion and S_{BET} value in comparison to other samples. Although numerous studies have been carried out to optimize the synthesis parameters such as temperature, time, pH and ligand type, there are limited reports on the effect of inorganic salt on the photocatalytic performance of MOFs [8a, 11c, 14,15] . Table 2 is compared efficiency of the prepared MOFs in organic pollution degradation with the literature. It is obvious that photocatalytic performance of sample D as optimum sample (> 95% dye degradation after 2h) is thoroughly comparable with the previous reports.

Table 2. Comparison of photocatalytic performance with the literature

Photo catalyst	Contaminants	Degradation efficiency [%]	Time [min]	Reference
MIL-100(Fe)	Basic Blue 41	98.2	180	[2b]
MIL-53 (Al)/Ag/AgCl(10%)	Rhodamine B	80-100	90	[2c]
Fe(bpydc [a])	Phenol	>90	60	[3c]
MIL-53(Fe)	Acid Orange7	~100	90	[8a]
MIL-88 A	Orange G	96.4	150	[13]
MIL-88 A	Rhodamine B	98	50	[14]
MIL-53 (Fe)	Orange G	~100	90	[15]
MIL-53(Fe)	Orange G	98	120	[27]
MIL-53(Fe)	Rhodamine B	> 95	20	[28]
Fe-MOFs	Acid Orange7	97	240	[29]
Fe-MOFs	Rhodamine B	90	90	[30]
Fe-MOFs	Congo red	96.97	300	[31]
Fe(III)-MOFs	OrangeⅡ	97.7	300	[32]
MIL-53(Fe)	Methylene Blue	>95	120	**present study**

[a] 2,2′-bipyridine-5,5′-dicarboxylate

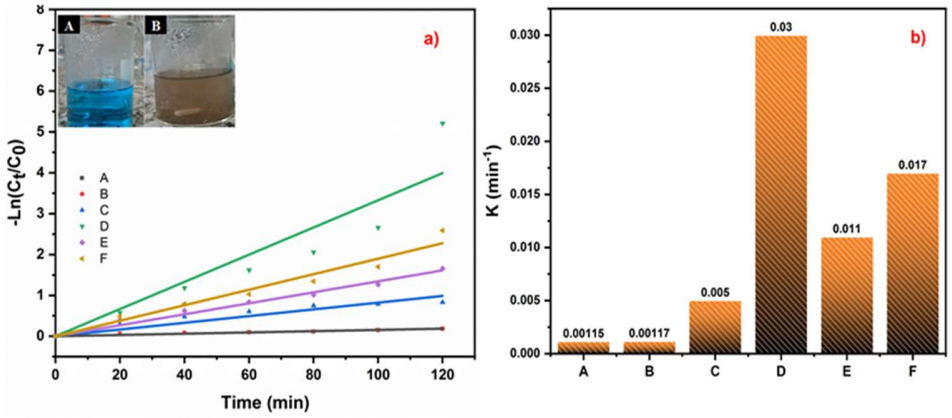

Figure 9. (a) The corresponding photo degradation kinetics of methylene blue with different photocatalysts (inset shows the dye solution before (A) and after (B) dye removal) (b) Comparison of different photocatalysts reaction rate constants for MB degradation

To study the possible degradation mechanism, H_2O_2 was utilized without photocatalysts to evaluate the degradation ability of hydrogen peroxide. As can be observed in Figure 8, H_2O_2 did not degrade MB appropriately. However, adding the

photocatalysts powder, degradation rate of dye dramatically increased. This indicates that optimum efficiency can be achieved when photocatalysts and H_2O_2 are used concurrently. Synthesized photocatalysts can be excited under visible light irradiation. Subsequently, excited photocatalysts generate electrons (e^-) and holes (h^+) in conduction and valence band. The presence of H_2O_2 may spark generation of active species $OH^·$ when hydrogen peroxide is exposed to light. In addition, H_2O_2 causes electron trapping and it is known as a barrier to restrain electron and hole recombination[33]. Equations (6,7) and (8,9) show the activation mechanism of MIL-53(Fe) and H_2O_2, respectively [26]. The Butler and Ginley equations (Eqn (4,5)) were used to estimate the conduction band edge potential (E_{CB}) and the valence band edge potential (E_{VB}).

$$E_{VB} = 0.5\,E_g + \chi - E_e \qquad (4)$$

$$E_{CB} = E_{VB} - E_g \qquad (5)$$

Where E_g is the band gap of synthesized powders calculated by the Tauc equation (Eqn (1)) (2.7 eV), χ is the absolute electronegativity of MIL-53(Fe) (5.55 eV), E_e is the free energy of free electrons (E_e ~4.5 eV for normal hydrogen electrode) [16 d]. According to mentioned equations, VB and CB edge potentials of MIL-53(Fe) were estimated approximately 2.4 V and –0.3 V respectively with respect to the NHE at pH= pH_{zpc}.

$$\text{MIL-53(Fe)} + hv \rightarrow h^+ + e^- \qquad (6)$$

$$CB^- + H_2O_2 \rightarrow OH^- + OH^· \qquad (7)$$

$$O_2^{-·} + H_2O_2 \rightarrow OH^- + OH^· + O_2 \qquad (8)$$

$$H_2O_2 + hv \rightarrow 2\,OH^· \qquad (9)$$

Intending to cover the whole part of dye degradation process it should be considered that the photocatalytic dye degradation mechanism for cationic dye like MB is different from the route for anionic ones. In contrary to anionic dyes , hydroxyl radicals do not have major role in cationic pollutants degradation. In terms of importance, N-de-ethylation reactions have privilege to degrade MB (Fig.8). In other words, MB is involved in surface controlled N-de-ethylation reactions which could be directly related with surface area of photo catalysts and H_2O_2 assists the enhancement of degradation process [34,25e]. Considering to mentioned terms and possible degradation mechanism, it could be concluded that any experimental path that leads to the increasing of photocatalysts surface area boosts the photo degradation. Performance stability is one of the significant concerns considered for photo catalysts as they are used in practical application. The cycling performance of sample (D) as optimized powder was assessed for three times by conducting repeatedly photocatalytic reaction under tungsten halogen lamp. Figure 10(c) illustrates that the photo catalyst did not have significant change in photo activity and degradation of MB through each cycle, indicating the sample (D) had sustainable act and retained a similar photocatalytic activity for more than 360 min. To

further confirmation, the structural and molecular analysis was done by XRD (Figure 10(a)) and FTIR spectra (Figure 10(b)). The results show that there is not remarkable change in the structure property of powders after three times reactions.

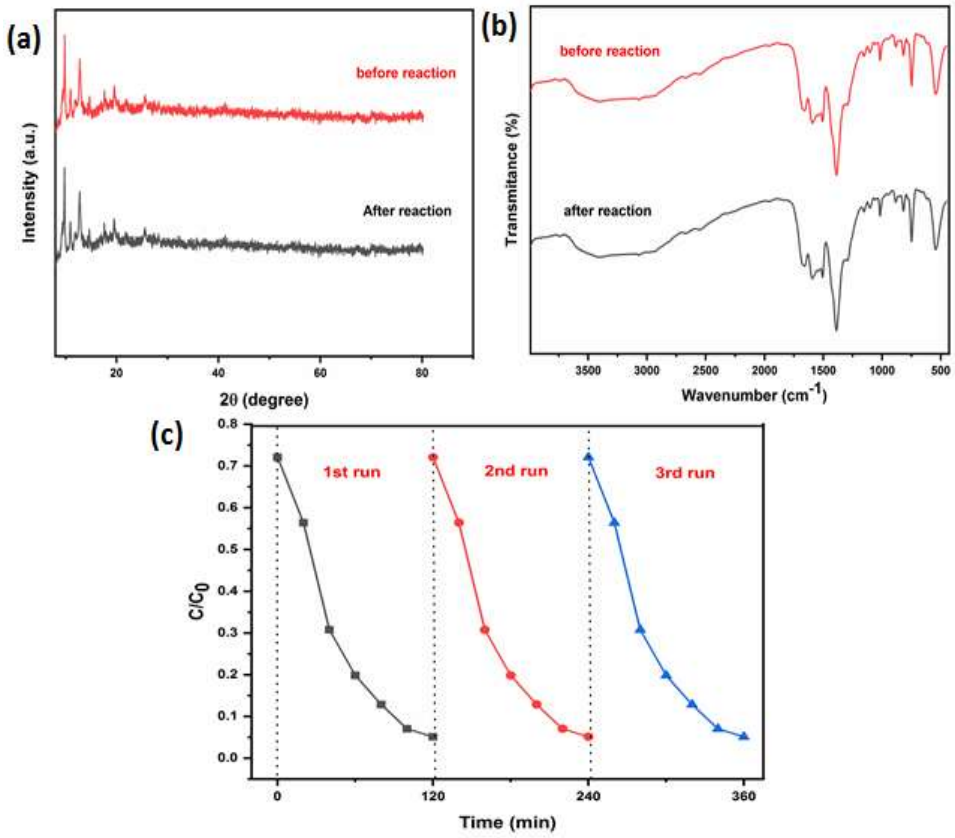

Figure 10. XRD pattern of MIL-53(Fe)-Chloride salt/120 ºC (D) before and after photocatalytic reaction (a), FTIR of the sample (D) before and after photocatalytic test (b), Recycling test on the MB degradation in sample (D) / H_2O_2 system (c)

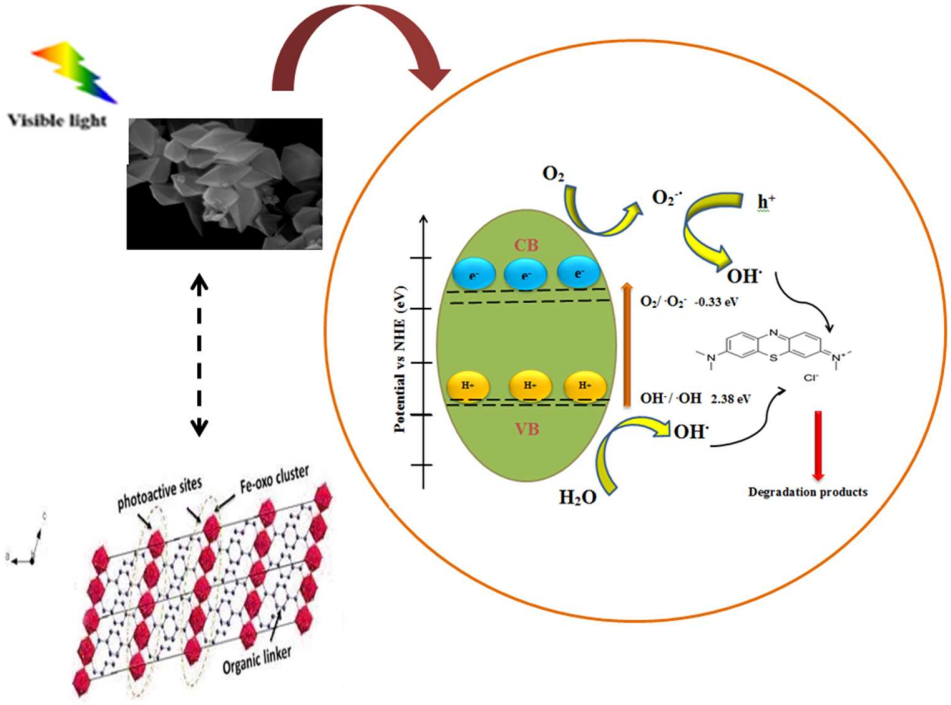

Figure 11. Schematic of possible dye degradation mechanism of methylene blue on the surface of MIL-53(Fe)

Conclusions

In the present study, MIL-53(Fe) was prepared for MB removal using different metal sources and temperatures via a facile solvothermal method. The effect of different conditions on efficiency of dye removal was investigated. Results demonstrated that the powder synthesized using iron chloride showed the best performance for dye degradation under visible light irradiation. Moreover, findings revealed that 120 ºC was the optimum temperature for preparing the photocatalysts. The main reason behind the higher photocatalytic performance could be attributed to L-H mechanism and more accessible surface of the particles to contact with pollutants. This study may help future researches on environmental fields to utilize high performance MOF-based photocatalysts for water treatment.

Experimental

Materials

Nitrate salt ($Fe(NO_3)_3 \cdot 9\ H_2O$), chloride salt ($FeCl_3 \cdot 6\ H_2O$), dimethylformamide (DMF), benzene dicarboxylic acid (BDC), and MB were purchased from Merck and used as received without further purification. All materials used in this experiment are available in analytical grade.

Powder synthesis

2.2.1. Particles obtained from nitrate salt source

To prepare iron nitrate solution, a certain amount of nitrate salt (5.655 g) was added into 36 mL of DMF. Then, 2.24 g of BDC was added into the same amount of DMF. Each of the solutions was put on a stirrer at 50 ºC and 1000 rpm for 20 min. Subsequently, the prepared solutions were poured into an autoclave and kept at 150 ºC for 12 h. The synthesized powders prepared at 120, 150, and 180 ºC were coded as (A), (B), and (C).

Particles obtained from chloride salt source

In the first step, stock solution was prepared adding a certain amount of $FeCl_3 \cdot 6H_2O$/ BDC/DMF with a molar ratio of 1:1:60. Subsequently, the prepared yellow solution was put on a stirrer at 50 ºC for 20 min and 1000 rpm to be homogenized. Finally, the solution was poured into a 110 mL autoclave for 12 h at 150 ºC. The resulting product was placed into 100 mL water for 24 h to be washed; then, the final product was extracted from water by centrifuging at 6000 rpm for 4 min. Finally, the powder was dried at 60 ºC for 16 h. This process was repeated 2 times but at different synthesis temperatures (120 and 180 ºC). The synthesized powders were labelled as (D), (E), and (F) for 120, 150, and 180 ºC, respectively. Subsequently, to wash the powders, the same process as mentioned for previous samples was carried out.

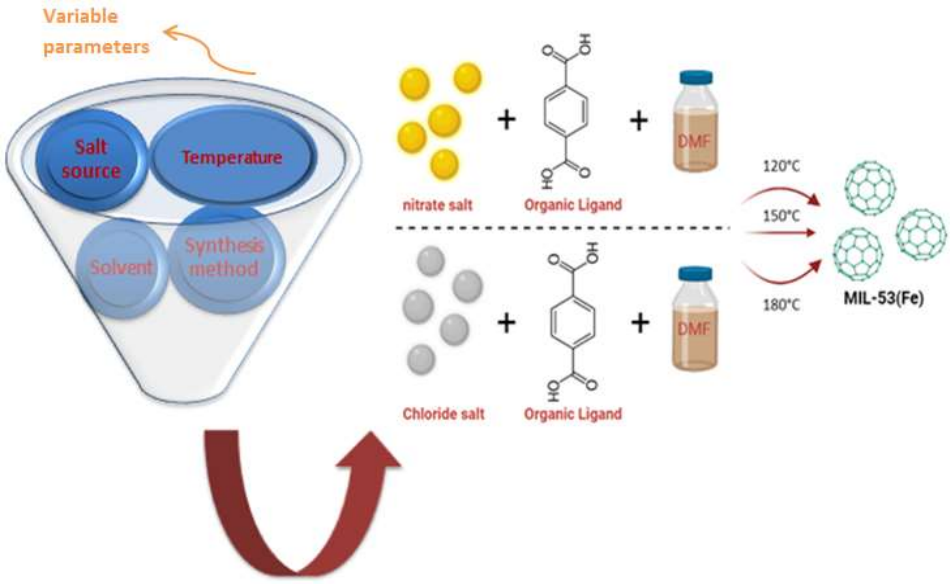

Figure 12. Schematic illustration for the preparation process of MIL-53(Fe) via solvothermal method

Powder characterization

To analyze the powders, X-ray diffraction (XRD) was used and the patterns of samples were collected by Inel Equinox 3000 X-Ray diffractometer (Cu Kα radiation (λ=1.54190 A˚) with scanning angle range from 5 to 80)) at a scanning rate of 6 º min^{-1} and a step size of 0.02º. Scanning Electron Microscopy (SEM; Stereoscan S 360 Cambridge) was employed to study the morphology of samples. Dynamic Light Scattering (DLS) were taken with (DLS:Cordouan-Wallis). Furthermore, Fourier transform infrared spectroscopy (FT-IR: Perkin Elmer) was performed on pellets of the synthesized particles diluted with KBr. The Brunauer–Emmett–Teller (BET) method was used to analyze surface area of the powders. To investigate the optical properties of the samples, UV-vis diffuse reflectance spectra (DRS) of the powders were collected using a UV-Vis spectrophotometer (JENWAY 6715).

Evaluation of samples photocatalytic performance

To evaluate the photocatalytic degradation of dye by the synthesized powders, 50 mg of each photocatalyst was added to 70 mL of a 5 $mg.L^{-1}$ MB solution. Subsequently, to establish adsorption/desorption equilibrium, the prepared solution was stirred (at 500 rpm) for 60 min in the dark at room temperature. Afterwards, a certain concentration of H_2O_2 was added to the solution. Then, while the temperature of the solution was kept constant, the dye solution was irradiated by a 500 W tungsten halogen lamp with a cut-off filter (λ < 700 nm). Eventually, The concentration of MB was detected using a UV-Vis spectrophotometer (JENWAY 6715) at its maximum absorption wavelength (554 nm). The concentration of MB was measured at a specific time.

Acknowledgements

The authors would like to acknowledge Color & Polymer Research Center (CPRC) for helping us in this research.

Keywords: Dye degradation, Environment, Iron-based MOFs, Metal-organic frameworks, Water treatment

References

[1] a) M. Kadhom, B. Deng. *Appl Mater Today*. **2018**, *11*, 219-230 ; b) A. Ali, M. Muslim, I. Neogi, M. Afzal, A. Alarifi, M. Ahmad, *ACS omega.* **2022**, *7*, 24438-24451; c) H. Sameie, A. A. S. Alvani, N. Naseri, F. Rosei, G. Mul, B. T. Mei. *Journal of* Electrochem. Soc. **2018**, *165*, H353 ; d)T. Mandal, S. Maity, D. Dasgupta, S. Datta. *Desalin.* **2010**, *250*, 87-94.

[2] a) R. Salimi, A. A. S. Alvani, N. Naseri, S. F. Du, D. Poelman. *New J. Chem* . **2018**, *42*, 11109-11116 ; b) N. M. Mahmoodi, J. Abdi, M. Oveisi, , M. A. Asli, M. Vossoughi. *Mater. Res. Bull.* **2018** , *100*, 357-366 ; c) V. PViswanathan, K. S. Divya, D. P. Dubal, N. N. Adarsh, S. Mathew. *Dalton Trans.* **2021**, *50*, 2891-2902.

[3] a) C. Wang, J. Kim, V. Malgras, J. Na, J. Lin, J. You, M. Zhang, J. Li, Y. Yamauchi. *Small*. **2019**,*15*, 1900744 ; b) V. P. Viswanathan, V. T. Balakrishnan, N. N. Adarsh, V. B. Varghese, S. Mathew. *Crystals.* **2023**,*13*, 47; c) Y. Li, H. Liu, W. J. Li, F.Y. Zhao, W. J. Ruan. *RSC Adv.* **2016,** *6*, 6756-6760 ; d) V. K. Sharma, M. Feng. A review. *J. Hazard. Mater.* **2019**, *372*, 3-16.

[4] a) X. Yang, Q. Xu. *Cryst. Growth Des* . **2017**, *17*, 1450-1455 ; b) C. Duan, H. Zhang, F. Li, J. Xiao, S. Luo, H. Xi. *Soft matter.* **2018**,*14*, 9589-9598

[5] a) R. Medishetty, J. K. Zaręba, D. Mayer, M. Samoć, R. A. Fischer. *Chem. Soc. Rev*. **2017**,*46*, 4976-5004 ; b) T. C. Wang, F. P. Doty, A. I. Benin, J. D. Sugar, W. L. York, E. W. Reinheimer, V. Stavila, M. D. Allendorf. *Chem. Commun* . **2019**, *55*, 4647-4650.

[6] a) N. Yin, K. Wang, Z. Li. *Desalin.* **2018**, *430*, 120-127 ; b) R. Liu, L. Chi, X. Wang, Y. Wang, Y. Sui, T. Xie, H. Arandiyan. *Chem. Eng. J.* **2019**, *357*, 159-168.

[7] a) A-Na. Dou, L-Bo. Yang, X-Dan. Fang, Q. Yin, M-Dong. Li, J. Li, M-Yan. Wang, A-Xin. Zhu, Q-Qing. Xu. *CrystEngComm.* **2018**, *20*, 3609-3619 ; b) Y. Zhang, C. Jia, Q. Wang, Q. Kong, G. Chen, H. Guan, C. Dong. *Ind. Eng. Chem. Res.* **2019**, *58*, 9450-9457.

[8] a) Y. Gao, S. Li, Y. Li, L. Yao, H. Zhang. *Appl. Catal. B.* **2017**, *202*, 165-174 ; b) T. Zeng, L. Wang, L. Feng, H. Xu, Q. Cheng, Z. Pan. *Dalton Trans.* **2019**, *48*, 523-534 ; c) Y. Zhang, J. Zhou, X. Chen, L. Wang, W. Cai. *Chem. Eng. J.* **2019**, *369*, 745-757.

[9] a) J. o. Liu, X. F. Li, C. Ying, G. Júlio CS da Silva, A. L. Barros, S. Alves-Jr, B. H. Li, F. Ren, S. R. Batten, T. A. Soares. *Dalton Trans.* **2015**, *44*, 19370-19382 ; b) M. Vassaki, K. E. Papathanasiou, C. Hadjicharalambous, D. Chandrinou, P. Turhanen, D. Choquesillo-Lazarte, K. D. Demadis. *Chem. Commun.* **2020**, *56*, 5166-5169.

[10] H. Li, M. Eddaoudi, M. O'Keeffe, O. M. Yaghi. *Nature*.**1999**, *402*, 276-279.

[11] a) X. Liu, Y. Zhou, J. Zhang, L. Tang, L. Luo, G. Zeng. *ACS Appl. Mater. Interfaces.* **2017**, *9*, 20255-20275 ; b) H. Chen, Y. Liu, T. Cai, W. Dong, L. Tang, X. Xia, L. Wang, T. Li. *ACS Appl. Mater. Interfaces.* **2019**, *11*, 28791-28800. c) D. Wang, H. Li, Q. Han, W. Jiang, C. Liu, G. Che. *J. Phys. Chem. Solids.* **2021**, *154*, 110027 ; d) Q. Zhao, L. Zhang, X. Wang, X. Jia, P. Xu, M. Zhao, R. Dai. *Transition Met. Chem.* **2019**, *44,* 789-797

[12] D. Wang, F. Jia, H. Wang, F. Chen, Y. Fang, W. Dong, G. Zeng, X. Li, Q. Yang, X. Yuan. J. *Colloid Interface Sci.* **2018**, *519*, 273-284.

[13] J. Wang, J. Wan, Y. Ma, Y. Wang, M. Pu, Z. Guan. *RSC Adv.* **2016**, *6*, 112502-112511.

[14] V. P. Viswanathan, S. V. Mathew, D. P. Dubal, N. N. Adarsh, S. Mathew. *ChemistrySelect.* **2020**, *5*, 7534-7542.

[15] M. Pu, Z. Guan, Y. Ma, J. Wan, Y. Wang, M. L. Brusseau, H. *Chi. Appl. Catal. A*. **2018**, *549*, 82-92.

[16] a) P. Horcajada, T. Chalati, C. Serre, B. Gillet, C. Sebrie, T. Baati, J. F. Eubank. *Nat. Mater 9*. **2010**, *9*, 172-178 ; b) X. Li, Z. Zeng, G. Zeng, D. Wang, R. Xiao, Y. Wang, C. Zhou. *J. Colloid Interface Sci.* **2020**, *561*, 501-511; c) Q. Wu, Y. Liu, H. Jing, H. Yu, Y. Lu, M. Huo, H. Huo. *Chem. Eng. J.* **2020**, *390*, 124615 ; d) G. Chaturvedi, A. Kaur, S. Kumar Kansal. *J. Phys. Chem. C.* **2019**,*123*, 16857-16867.

[17] a) P. Horcajada, C. Serre, G. Maurin, N. A. Ramsahye, F. Balas, M. Vallet-Regi, M. Sebban, F. Taulelle, G. Férey. *J. Am. Chem.* **2008**, *130*, 6774-6780 ; b) M. Ghanbarian, S. Zeinali, A. Mostafavi. *Sens. Actuators, B.* **2018**, *267*, 381-391; c) S. He, T. Li, L. Zhang, X. Zhang, Z. Liu, Y. Zhang, J. Wang, H. Jia, T. Wang, L. Zhu. *Chem. Eng. J*. **2021**, *424*, 130515 ; d) A. Banerjee, R. Gokhale, S. Bhatnagar, J. Jog, M. Bhardwaj, B. Lefez, B. Hannoyer, S. Ogale. *J. Mater. Chem.* **2012**, *22*, 19694-19699.

[18] a) T. Chalati, P. Horcajada, R. Gref, P. Couvreur, C. Serre. *J. Mater. Chem.* **2011**, *21*, 2220-2227 ; b) H. Wu, M.-Dan. Ma, W-Zhuo. Gai, H. Yang, J-Ge. Zhou, Z. Cheng, P. Xu, Z-Yan. Deng. *Environ. Sci. Pollut. Res.* **2018**, *25*, 27196-27202 ; c) N. Liu, W. Huang, X. Zhang, L. Tang, L. Wang, Y. Wang, M. Wu. *Appl. Catal. B.* **2018**, *221*, 119-128.

[19] J. Gordon, H. Kazemian, S. Rohani. *Microporous Mesoporous Mater.* **2012**, *162*, 36-43.

[20] G-Thanh. Vuong, M-Hao. Pham, T-On. Do. *CrystEngComm.* **2013**, *15*, 9694-9703.

[21] a) Y. Zhang, J. Zhou, J. Chen, X. Feng, W. Cai. *J. Hazard. Mater.* **2020**, *392*, 122315 ; b) R. Salimi, H. Sameie, A. A. Sabbagh Alvani, A. A. Sarabi, H. Eivaz Mohammadloo, F. Nargesian, M. Sabbagh Alvani, M. Tahriri, *JOSA B.* **2013**, *30*, 1747-1754.

[22] a S.R. Elliott, Physics of amorphous materials, vol. 20 (*Burnt Mill, Harlow, Essex CM*), *Longman Group, Longman House, E ; b)* R. Salimi, H. Sameie, A. A. Sabbagh Alvani, A. A. Sarabi, F. Moztarzadeh, M. Tahriri, *Luminescence*. **2011**, *26*, 449-455 ; c) R. Salimi, H. Sameie, A. A. Sabbagh Alvani, A. A. Sarabi, F. Moztarzadeh, H. Eivaz Mohammadloo, F. Nargesian, M. Tahriri, *J. Mater. Sci.* **2012**, *47*, 2658-2664.

[23] a) C. MA. Parlett, K. Wilson, A. F. Lee. *Chem. Soc. Rev.* **2013**, *42*, 3876-3893 ; b) T. Xiong, F. Dong, Z. Wu. *RSC Adv.* **2014**, *4*, 56307-56312.

[24] W. Wang, J. Zhou, Z. Zhang, J. Yu, W. Cai. *Chem. Eng. J.* **2013**, *233*, 168-175.

[25] a) M. Muruganandham, M. Swaminathan. *Dyes Pigm.* **2006**, *68*, 133-142 ; b) I. Poulios, E. Micropoulou, R. Panou, E. Kostopoulou. *Appl. Catal. B.* **2003**, *41*, 345-355 ; c) S. Zhou, A. K. Ray. *Ind. Eng. Chem. Res.* **2003**, *42*, 6020-6033 ; d) R. W. Matthews. *J. Phys. Chem.* **1987**, *91*, 3328-333; e) C-chen. Wang, J-Rong. Li, X-Liang. Lv, Y-Qiu. Zhang, G. Guo. *Energy Environ. Sci.* **2014**, *7*, 2831-2867.

[26] J. Saien, S. Khezrianjoo. *J. Hazard. Mater.* **2008**, *157*, 269-276.

[27] M. Pu, Y. Ma, J. Wan, Y. Wang, J. Wang, M. L. Brusseau. *Catal. Sci.Technol.* **2017**, *7*, 1129-1140.

[28] W. Mei, D. Li, H. Xu, J. Zan, L. Sun, Q. Li, B. Zhang, Y. Wang, D. Xia. *Chem. Phys. Lett.* **2018**, *706*, 694-701.

[29] X. Li, W. Guo, Z. Liu, R. Wang, H. Liu. *Appl. Surf. Sci.* **2016**, *369*,130-136.

[30] D. Pattappan, S. Vargheese, K. V. Kavya, R. R. Kumar, Y. Haldorai. *Chemosphere.* **2022**, *286*, 131726.

[31] F. Wei, D. Chen, Z. Liang, S. Zhao. *Nanomater.* **2018**, *8*, 248.

[32] D. Chen, P. F. Feng, F. H. Wei. *Chem. Eng. Process -process Intensification.* **2019** *135*, 63-67.

[33] a) Y. Gao, G. Yu, K. Liu, S. Deng, B. Wang, J. Huang, Y. Wang. *Chem. Eng. J.* **2017**, *330*, 157-165 ; b) N. Liu, W. Huang, M. Tang, C. Yin, B. Gao, Z. Li, L. Tang, J. Lei, L. Cui, X. Zhang. *Chem. Eng. J* .**2019**, *359*, 254-264.

[34] a) T. Watanabe, T. Takizawa , K. Honda. *J. Phys. Chem* .**1977**, 81, 1845–185 ; b) Z. T. Yu, Z. L. Liao, Y. S. Jiang, G. H. Li , J. S. Chen. *Chem. Eur. J.* **2005**, 11, 2642–2650.

TOC Graphic

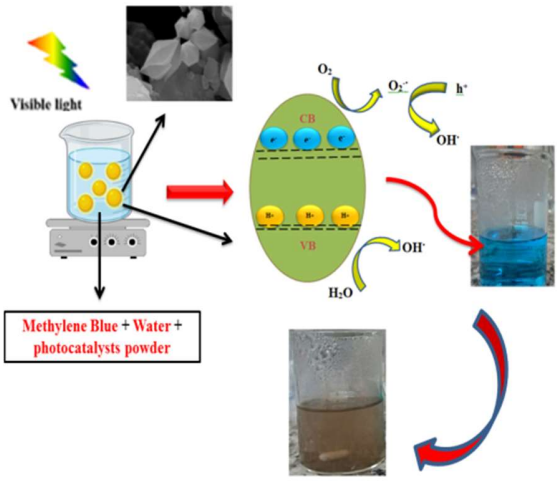

TOC Text

The MIL-56 (Fe) series were prepared to be manipulated for water treatment. The results showed the temperature and the inorganic salt sources directly affect the final efficiency due to the different surface area of the samples described by Langmuir-Hinshelwood (L-H) mechanism.